Author(s): Lind, Leevi; Laamanen, Hannu; Pölönen, Ilkka

Title: Hyperspectral imaging of asteroids using an FPI-based sensor

Year: 2021

Version: Accepted version (Final draft)

Please cite the original version:

Lind, L., Laamanen, H., & Pölönen, I. (2021). Hyperspectral imaging of asteroids using an FPI-based sensor. In S. R. Babu, A. Hélière, & T. Kimura (Eds.), Sensors, Systems, and Next-Generation Satellites XXV (Article 118580F). SPIE. Proceedings of SPIE : the International Society for Optical Engineering, 11858. https://doi.org/10.1117/12.2599514

Hyperspectral imaging of asteroids using an FPI-based sensor

Leevi Lind[a], Hannu Laamanen[b], and Ilkka Pölönen[a]

[a]University of Jyväskylä, Faculty of Information Technology, Jyväskylä, Finland
[b]University of Eastern Finland, Department of Physics and Mathematics, Joensuu, Finland

ABSTRACT

The compositions of asteroids are of interest for the planetary sciences, mining, and planetary defense. The main method for evaluating these compositions is reflectance spectroscopy. Spectroscopic measurements performed from Earth can not resolve how different materials are distributed on the asteroids, making flyby– and rendezvous missions necessary for obtaining detailed information. Using the CubeSat platform could reduce the costs of these missions, but it also sets constraints on the payload mass and volume. One small and light instrument capable of producing spatially resolved spectral data is a hyperspectral imager based on the Fabry-Perot interferometer. This work proposes a method of calculating reflectance data from hyperspectral radiance images of an asteroid and a computationally evaluated incident spectral radiance. The proposed method was tested in laboratory conditions with inconclusive results. The obtained reflectances differed from reference measurements, but we believe this was caused by improper calibration of the used imager rather than errors in the method itself.

Keywords: Hyperspectral imaging, imaging spectroscopy, asteroid, reflectance imaging, CubeSat, FPI

1. INTRODUCTION

Asteroids are defined as small, natural, solid bodies orbiting the Sun, differing from comets in that they do not expel a tail of gas or dust.[1] The compositions of asteroids are of interest in the planetary sciences by offering information about the evolution of our solar system, and the effects of space weathering.[2,3] Other fields interested in this compositional information are those of asteroid mining[4,5] and planetary defense.[3] For mining, surveying the materials present in an asteroid before starting mining operations is naturally valuable. In planetary defense, meaning protecting Earth from potentially hazardous objects, the composition of an asteroid can affect how to best alter its trajectory.

One of the most important techniques in analyzing the compositions of asteroids is reflectance spectroscopy: comparing the spectral distribution of light reflected by the asteroid to the spectral distribution of sunlight incident on it.[1] When performing measurements from Earth, the spectral measurements are "disc-integrated": the asteroids are seen as uniform discs due to their small size.[6] For more detailed analysis, flyby– and rendezvous missions, such as NASA's NEAR-Shoemaker[7] and OSIRIS-REx,[8,9] and JAXA's Hayabusa2,[10] are needed. While the main objectives of OSIRIS-REx and Hayabusa2 were to retrieve a sample back to Earth, they also performed spatially resolved spectroscopic measurements on their respective target asteroids.

In recent years the CubeSat[11] platform has provided a standardized and affordable solution for space research in the form of nanosatellites. Missions utilizing the CubeSat design have also ventured into the "deep-space" outside of Earth's atmosphere, beginning with the Mars Cube One (MarCO) accompanying the InSight Mars lander.[12] ESA is currently developing two asteroid missions involving CubeSats: the Miniaturised – Asteroid Remote Geophysical Observer (M-ARGO)[13] and Hera.[3,14] M-ARGO is a standalone 12-unit CubeSat, while Hera involves a larger spacecraft carrying two 6-unit CubeSats, Juventas[15] and Milani.[16]

Hera, previously known as the Asteroid Impact Mission (AIM), is the European component of the Asteroid Impact and Deflection Assessment (AIDA). This mission is a joint effort by ESA and NASA, the North American component going by the name of Double Asteroid Redirection Test (DART). The mission targets the asteroid 65803 Didymos,[17] a near-Earth object (NEO) consisting of a main body (Didymos) and its satellite (Dimorphos).

Further author information: L.L.: E-mail: leevi.j.j.lind@jyu.fi

DART is a kinetic impactor set to collide with Dimorphos, altering its orbit around Didymos. Hera will arrive at the scene three years later to observe the aftermath of the DART collision and characterize the properties of Didymos through various techniques. One of these techniques is spatially resolved reflectance spectroscopy, in this paper referred to as hyperspectral imaging. The task of imaging is delegated to one of Hera's companion CubeSats, Milani.

Milani's main scientific payload is the ASPECT imaging suite consisting of three instruments with different wavelength ranges: two hyperspectral imagers (HSI) for visible light and near-infrared (NIR), and a point spectrometer for short-wave infrared (SWIR). All three devices are based on the Fabry-Perot interferometer (FPI), and the two HSIs are frame-based devices, recording intact frames and varying the recorded wavelength over time. FPI-based HSIs can be made very light and compact, making them well suited for nanosatellite applications. The spaceworthiness of this imager design has been proven on two Finnish Earth observation CubeSats, the Aalto-1[18] and the Reaktor Hello World.[19]

While spatially resolved reflectance spectroscopy, hyperspectral imaging, has been done on previous asteroid missions, the instruments have been different from the FPI-HSIs onboard Milani. For instance, on OSIRIS-REx the imager was essentially a whiskbroom camera: a point spectrometer with movable optics for scanning its field of view over a target area. This paper aims to answer the question of how to produce reflectance data from hyperspectral images of asteroids taken with frame-based FPI-HSIs. Our main focus is the Milani and the ASPECT imager onboard it, but the methods and considerations presented here should apply to other asteroid missions employing frame-based HSIs.

2. MATERIALS AND METHODS

2.1 Theoretical Background

The FPI-HSIs this work considers are based on using the FPI as a tunable transmission filter. The transmission spectrum of the FPI consists of sharp spikes, the central wavelengths of which depend on the cavity length of the device. With a known cavity length and a proper bandpass filter ("order sorting filter"), the transmitted light can be limited to a few peaks with well-known wavelengths. By modulating the cavity length, the transmission wavelengths can be changed. Recording the light transmitted by the FPI for a series of known cavity lengths will yield a spectral image. This imager concept is considered in more detail by Saari et al. in Ref. 20 and Ref. 21.

The quantity we refer to as reflectance in this work is more exactly known as the bidirectional reflectance factor (BRF), for which we follow the treatment of Manolakis et al.[22] The BRF of a surface is defined as the relation of light reflected from the surface and the light reflected from an ideal Lambertian reflector in identical geometry. Mathematically this can be expressed through radiance as

$$R_\lambda = \frac{L_{\lambda r}}{L_{\lambda id}}, \tag{1}$$

where R_λ denotes the BRF, $L_{\lambda r}$ is the radiance reflected from the sample, and $L_{\lambda id}$ is the radiance reflected from the ideal surface. The subscript λ denotes spectral quantities.

In a laboratory measurement, one can find the spatially resolved BRF rather easily with a hyperspectral imager. A typical procedure consists of imaging an approximately ideal Lambertian reflector, a "white sample", in addition to the actual imaging target. Dividing the hyperspectral image of the target with the hyperspectral image of the white sample according to Eq. (1) will then yield the BRF. Reflectance standards other a white one can also be used, and it is generally a good practice to use a standard with reflectance properties similar to the imaging target.[22]

For the imaging of asteroids, a physical reference sample is impractical. If one were to place a reflectance standard on or near the asteroid, the standard would have to be fairly large. For example, the imager onboard the Milani CubeSat has a requirement of 2 m / pixel for its spatial resolution.[23] This resolution would require the reflectance standard to be at least 2 meters in diameter, making it much larger than the 6-unit CubeSat itself. Including the reflectance standard and the equipment to deliver it to the target asteroid would increase the satellite's mass and the complexity of its operation.

Another approach would be to somehow suspend a reflectance standard between the imager and the asteroid, with a mechanism to move the standard in and out of the imager's field of view. This would again increase both the mass and the number of moving parts of the system: neither is desirable, especially in the context of autonomous CubeSat missions.

Instead of imaging a physical reflectance standard we propose to calculate the radiance that would be reflected from an ideal Lambertian disc placed on the asteroid: an imaginary white sample. In the proposed model, the only light source contributing to light reflected from the asteroid is the Sun, and the light incident on the asteroid is considered approximately collimated. The propagation medium between the Sun and the asteroid, and between the asteroid and the HSI, is modeled as vacuum with no absorption.

To calculate the spectral radiance reflected from an ideal Lambertian sample, one must know the spectral irradiance incident on the sample and the incidence angle. The spectrum of sunlight has been well characterized also outside the Earth's atmosphere, and datasets of this spectrum are available, for example, from the National Renewable Energy Laboratory of the United States (NREL).[24] This irradiance spectrum is measured near Earth at a distance of one Astronomical Unit (AU) from the Sun, but it can be scaled for other heliocentric distances through the inverse square law. In the proposed model, the imaginary white sample is a flat disc placed perpendicular to the direction of light traveling from the asteroid to the HSI. The incidence angle of sunlight on this disc is then given by the phase angle, the angle of Sun-object-observer, a measure often used in describing astronomical measurements. A schematic view of the measurement geometry is presented in Fig. 1.

Denoting the spectral radiance reflected from an ideal Lambertian sample with $L_{\lambda id}$, the spectral irradiance incident on that sample with $E_{\lambda i}$, and the phase angle of the measurement with ϕ, the spectral radiance can be expressed as

$$L_{\lambda id} = \frac{E_{\lambda i} \cos \phi}{\pi} \tag{2}$$

by using Lambert's cosine law. Applying the law of conservation of radiance, this reflected spectral radiance is the same that an HSI would detect, regardless of the distance between the asteroid and the HSI.

2.2 Experimental Work

To test the proposed method of producing reflectance data, a laboratory setup for modeling the imaging of asteroids was built. The central idea of the experiments was to apply the proposed white correction method for FPI-HSI data resembling that of asteroids and comparing the resulting reflectances to results of reference measurements. In addition to a rock sample standing in for an asteroid, some reflectance standards in the form of a ColorChecker and gray ceramic samples were measured. The imager used in the measurements was a prototype model built by the Technical Research Centre of Finland (VTT). It belongs to the same line of FPI-HSIs as the ones described by Saari et al. in Ref. 20 and Ref. 21 and works through the same operating principle. The wavelength range of the imager was 456 nm to 840 nm, and it recorded 133 wavelength channels with FWHMs
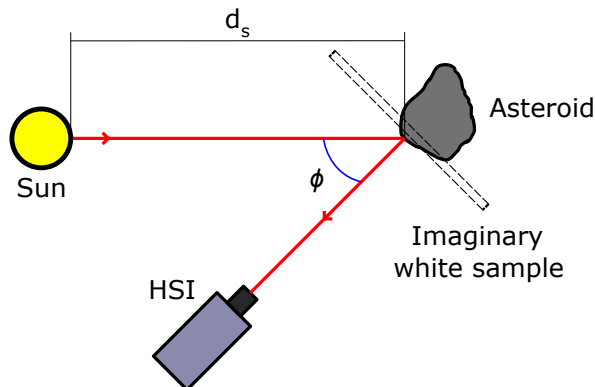

Figure 1: Measurement geometry for asteroid imaging.

ranging from 12 nm to 16 nm. The data was recorded from 80 separate exposures taken with different values of FPI cavity length. The imager's objective lens was exchangeable, but for all measurements related to this work, the lens was a Navitar machine vision objective with 35 mm focal length and $f/1.4$ aperture size.

Raw data captured with the HSI were converted to hyperspectral radiance images using `fpipy`,[25] a Python library developed at the University of Jyväskylä for processing data produced by FPI –based imagers. This conversion consisted of several steps, including the subtraction of dark current, demosaicing the HSI's RGB sensor data, and building a hyperspectral datacube of 133 wavelength channels out of the 80 raw data frames. The last of these relied on a calibration dataset provided by the manufacturer, including the FPI cavity lengths for each frame, the corresponding passing wavelengths, and calibration factors for the sensor's red, green, and blue pixels. The calibration and producing hyperspectral images from the raw data from this type of devices are considered in more detail in Ref. [20] and Ref. [21].

The measurement setup for modeling asteroid imaging consisted of a light source, a sample stage, the FPI-HSI, and a commercial spectroradiometer (Konica Minolta CS-2000[26]). While the HSI could measure up to 840 nm, the spectroradiometer's wavelength range was limited to 780 nm in the longer wavelengths. This constrained the usable HSI data to the range of 456 - 780 nm, which was covered by 115 wavelength channels. The aperture of the spectroradiometer was set to its lowest possible value of 0.1°. The used light source was an old slide projector (Leitz Pradovit 153). The projector was chosen for its high output power, approximately Sun-like spectrum (see Fig. 4(a)), and nearly uniform distribution of light on the illuminated area.

A schematic view and a photograph of the setup can be seen in Fig. 2. In the schematic of Fig. 2(a), the distance d_p is the distance between the light source and the sample, ϕ denotes the phase angle, and d_{HSI} is the distance between the sample and the hyperspectral imager. In all measurements, the distance d_{HSI} was approximately 30 cm, and the phase angle ϕ approximately 30°. As the projector output was not ideally collimated, the irradiance incident on the sample could be adjusted by modifying the distance between the projector and the sample, d_p. The sample stage and its immediate surroundings were covered with black cloth to reduce background reflections.

The rock sample was measured with eight levels of incident irradiance, achieved with eight values of projector–sample -distance d_p. The measurement sequence for the rock sample is presented as a flowchart in Fig. 3. The level of incident light was evaluated for each distance d_p by measuring the luminance reflected from a diffuse white sample, with its normal facing the projector. The luminance was converted to illuminance approximating the white sample as a Lambertian reflector and utilizing Lambert's cosine law. The photometric units of luminance and illuminance were used for their convenience: the CS-2000 spectroradiometer allowed simple and fast luminance measurements.

The obtained illuminance values were used for comparing the light levels in the measurements to those present in the imaging of asteroids. A reference value for the illuminance at a heliocentric distance of 1 AU was calculated using the Sun's irradiance spectrum[24] and the spectral sensitivity of the human eye (the $V(\lambda)$ –curve). The reference illuminance E_{Vref} was scaled to larger heliocentric distances through the inverse square law. The subscript V is used to distinguish the photometric units from their radiometric counterparts. The approximate heliocentric distance corresponding to each projector position was found by solving the equation

$$E_V = \frac{E_{Vref}}{d_s^2} \tag{3}$$

for the heliocentric distance d_s, with E_V denoting the measured illuminance. The evaluated heliocentric distances for all eight measurements are presented in Tab. 1 together with the corresponding projector-sample –distances, illuminance values, and total exposure times of the hyperspectral images.

The exposure times presented in the table were calculated by multiplying the exposure time of one frame by 80, the total number of frames captured for one hyperspectral image. In truth, this total exposure time would be slightly longer, as between frames the cavity length of the FPI must be adjusted. For actual asteroid missions, the capture times could be shorter than the presented results. According to a preliminary mission plan,[23] Milani's operations will be performed when the distance to the Sun is between 1.5 and 2.2 AU. The irradiance of incident sunlight on the asteroid will then, for the most part, be higher than in our laboratory tests,
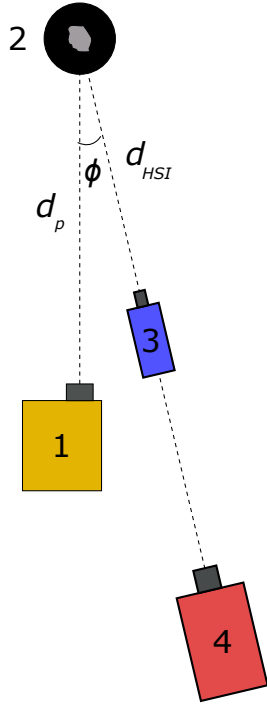
(a) Schematic view of the setup. 1 is the projector, 2 is the sample stage, 3 is the HSI, and 4 is the spectroradiometer.
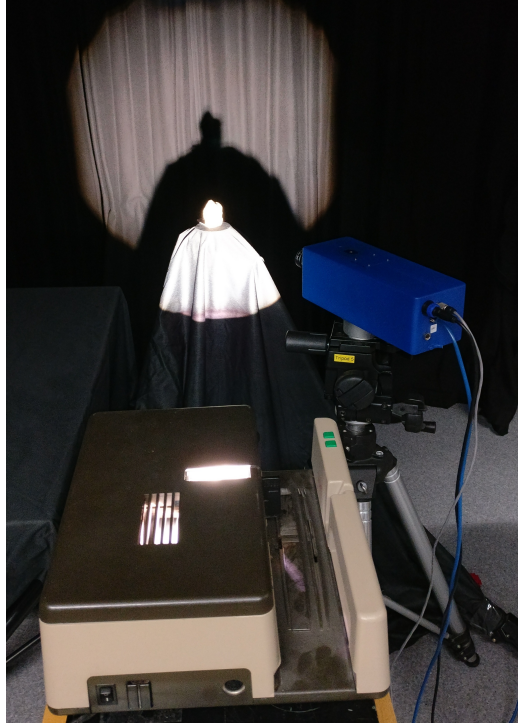
(b) Photograph of the setup showing the projector, the sample stage, and the HSI.

Figure 2: A schematic view and a photograph of the measurement setup for simulating asteroid imaging. The CS-2000 spectroradiometer is not visible in the photograph.

allowing a shorter exposure time. This holds if the f-number of Milani's imager is similar to that of the imager used in our experiments.

While Sec. 2.1 describes evaluating the radiance reflected from an ideal Lambertian sample through calculations, in the laboratory experiments this was not feasible. Instead, the reflected light was measured from a diffuse white sample in a similar geometry using the CS-2000 spectroradiometer placed behind the HSI. For each of the eight projector positions, a dataset of test reflectance R_{test} was produced by dividing the hyperspectral radiance image of the sample with the spectral radiance of the white sample, as measured using the spectroradiometer. To evaluate the performance of this method, a reference reflectance R_{ref} was calculated by dividing the same hyperspectral image of the sample with a hyperspectral image of the white sample.
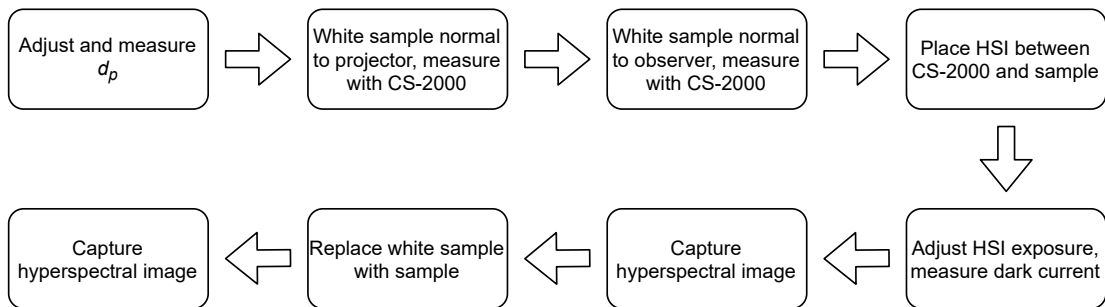

Figure 3: Measurement sequence as a flowchart for measurements of the rock sample.

Table 1: Projector-sample -distances d_p, illuminance values E_V, corresponding approximate heliocentric distances d_s, and total exposure times t_{tot} for measurements of the rock sample.

d_p [cm]	E_V [lx]	d_s [AU]	t_{tot} [s]
51	29 000	2.1	2.8
62	20 000	2.6	4.4
72	15 000	3.0	6.0
84	11 000	3.5	7.6
98	8 800	3.9	10.0
113	6 600	4.5	13.2
125	5 700	4.8	16.4
149	4 100	5.7	22.8

For the ColorChecker measurements, the measurement sequence differed slightly from that presented in Fig. 3: the sequence included an additional step of measuring the samples also using the CS-2000 spectroradiometer. Two ColorChecker cards were imaged, each with two colored patches visible in the image: one with green and blue, and the other with red and yellow. For measurements of both ColorChecker cards, the distance between the projector and the sample was 83 cm, and the illuminance incident on them was 12 klx. The datasets of test reflectance were produced similarly to those of the rock sample. The reference reflectances were calculated for each colored patch by dividing the spectroradiometer data of them with the corresponding spectroradiometer data of the white sample.

Two measurements of matte surfaced gray reflectance standards were made: one with a darker gray reflecting approximately 10 %, and one with a lighter gray reflecting approximately 30 %. The measurement sequence was changed by not including the step of measuring the white sample with the HSI. Test reflectance datasets were again produced by dividing the spectral radiance images of the samples with the corresponding spectral radiances of the white sample obtained with the spectroradiometer. The reference reflectances for the ceramic samples were measured using a commercial spectrophotometer (PerkinElmer Lambda 1050[27]).

3. RESULTS

Results of the experimental work are presented through various figures. First, Fig. 4 shows the spectral radiance measured from the white sample using the HSI and the CS-2000 spectroradiometer. The HSI data was averaged over a 100×100-pixel area at the sensors's center to reduce noise. Figure 4(a) gives the spectral radiances from both devices for one measurement, and Fig. 4(b) the relative deviation of spectral radiance between the two devices for all eight measurements of the stone.

In Fig. 4(b) the graph corresponding to the first measurement is similar to the others in shape, but not in magnitude. This could be explained as an oversight on the measurer's part: the light source may not have been allowed to stabilize sufficiently before the first measurement.
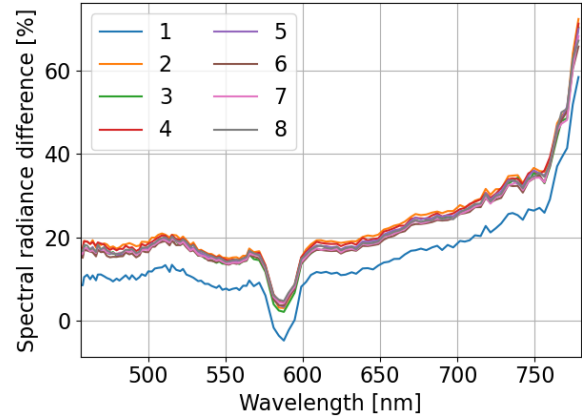
Both graphs of Fig. 4 point to errors in the radiances measured using the HSI, with the radiance seen by the HSI being in all measurements higher than that recorded with the spectroradiometer. If the first measurement is ignored, the radiance curves corresponding to measurements made with different illuminance levels are very similar. As such, the error behaves linearly, and it would likely be quite simple to remove it through calibration.

The dip in radiance near 580 nm is present in all measurements performed with the imager. It is likely caused by overlapping quantum efficiencies of the HSI's CMOS sensor's different colored pixels. Another notable feature is the increase in deviation toward longer wavelengths. Again, since both appear similar in measurements made with different illuminance levels, they could likely be corrected with proper calibration.

Figure 5 presents the test– and reference reflectances of the rock sample for two of the eight measurements. Full reflectance images were calculated as detailed in Sec. 2 and then averaged over a 100×100-pixel area near the sample's center to reduce noise. In both graphs, the test reflectance is higher than the reference reflectance, and it exhibits the same deviations near the wavelength of 580 nm and in the longer wavelengths as the radiance deviation curves of Fig. 4(b).
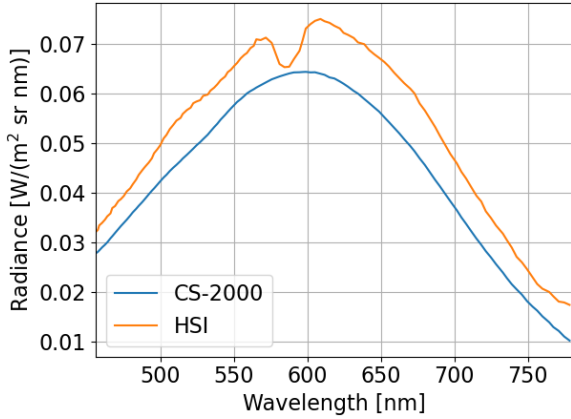
(a) Radiance of white sample, measurement 3   (b) Radiance difference in the 8 measurements
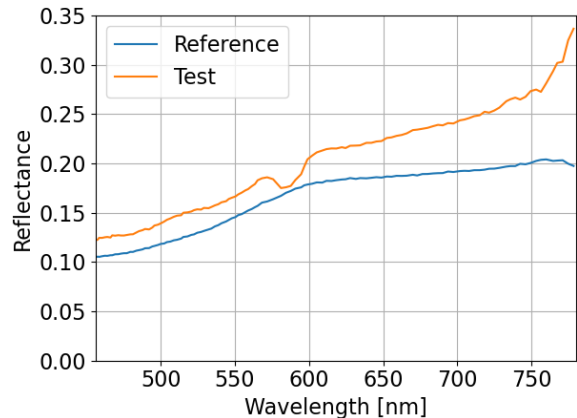
Figure 4: Radiance spectra of the white sample in measurement 3, as measured by the HSI and the spectroradiometer, and the radiance difference between white sample measurements performed with the HSI and the spectroradiometer for all eight measurements.

Data from the imager has previously been used by comparing the hyperspectral image of a target to a hyperspectral image of a white sample, both captured with the same imager. When the reflectance of the sample is calculated in this manner, errors in the device's ability to capture radiances present in both the sample data and the white reference data will cancel each other. If the sample image is compared to a white reference radiance derived from calculations in the unit of $W/(m^2\,sr\,nm)$, or from a calibrated device producing readings in the same unit, the errors of the sample image will be visible. Rigorous calibration of the imager is then more critical in this application than in a typical laboratory imaging setup.

Figure 5(a) also has a feature not visible in Fig. 5(b): a very sharp drop in both test- and reference reflectance near 570 nm. A similar effect was also observed in one other rock sample measurement at the same wavelength. As the feature is present in both test- and reference reflectances, it likely originates from the hyperspectral image taken of the rock sample. The hyperspectral radiance image of the rock sample was examined by sampling ten arbitrary points on the stone: the spectra of all ten points exhibited a similar drop at the same wavelength. Six of the eight measurements did not show this drop, leading us to believe that its cause was not in the reflectance
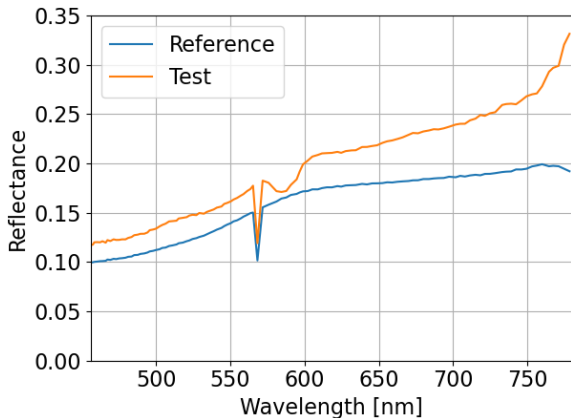
(a) Rock sample reflectance, measurement 2   (b) Rock sample reflectance, measurement 3

Figure 5: Rock sample reflectances from two measurements, averaged from a 100×100 pixel area near the center of the sample.

properties of the sample, but in the used imager. This spectral feature could be caused by inconsistent operation of the imager's FPI's piezo actuators responsible for controlling the cavity length.

The dataset of measurement 3 was selected for further analysis. With measurement 1 likely compromised by errors on the measurer's part and measurement 2 containing an unexpected dip in reflectance suspected to be caused by a malfunction of the HSI, measurement 3 had the highest incident irradiance on the sample of the remaining six measurements. This data was considered to best represent the real conditions of imaging asteroids. To examine the effect of brightness variation on the reflectance results, both test– and reference reflectance images were averaged over the wavelengths in each spatial pixel. The relation between average test– and reference reflectances is presented as a scatter plot in Fig. 6, with each point corresponding to one spatial pixel of the hyperspectral image. Pixels from the background were separated from those of the sample through masking by utilizing the `masked array` – module of the `numpy` -Python library.[28] The graph also contains a red line corresponding to an ideal result where the test– and reference reflectances would be in perfect alignment.

The test– and reference reflectances of the rock sample area appear to be related to each other linearly. While the slope of this linear trend does not exactly correspond to the ideal reference line, the linearity itself suggests that calibration of the results would not be overly difficult.

Measurements of the two ColorChecker cards yielded similar results, and thus only one of them is considered. Results from measurements of the card with green and blue patches are presented in Fig. 7: Fig. 7(a) considers the test– and reference reflectances of the green patch, and Fig. 7(b) the same for the blue patch, while Fig. 7(c) shows an RGB-reconstruction of the reflectance image. The test reflectance results were averaged over a 100×100-pixel areas to reduce noise. These areas are marked on the RGB image with white squares.

Results of the ColorChecker reflectance measurements share similarities with the results of the rock sample measurements. The test reflectance is again overall higher than the reference reflectance. The dip in reflectance near the wavelength of 580 nm is again visible, as is the rise in reflectance in the IR region. However, for the blue patch, the results appear markedly better than for the green one. This could be due to the area of interest being near the edge of the sensor, as opposed to its center. As shown in Fig. 4, the radiances captured with the HSI are higher than those captured with the spectroradiometer. Toward the edge of the sensor, vignetting caused by the HSI's optical system reduces the radiance, yielding results more in line with those of the spectroradiometer. Vignetting, as well as other properties of this particular imager, are considered in Ref. 29 through several characterization measurements.

As was the case for the ColorChecker measurements, measurements of the two gray ceramic reflectance standards did not greatly differ from each other. For this reason, only the lighter sample is considered here, with results related to it presented in Fig. 8. The test– and reference reflectance spectra are again plotted in
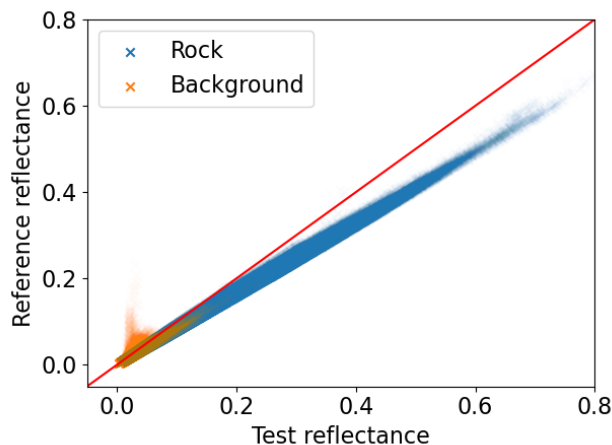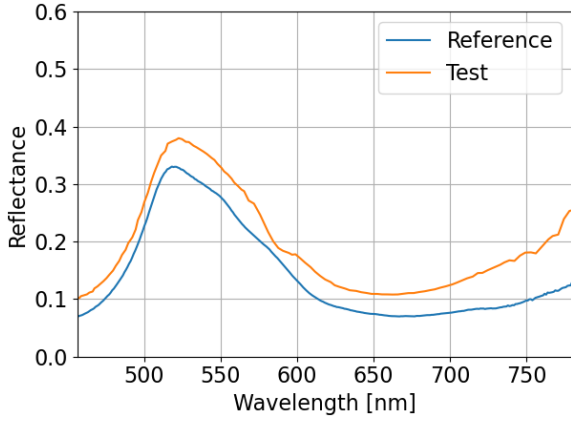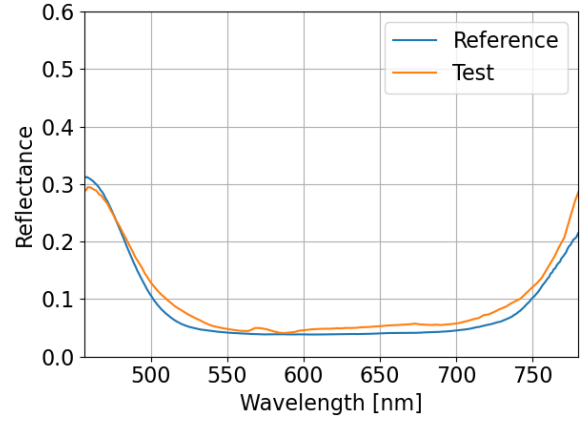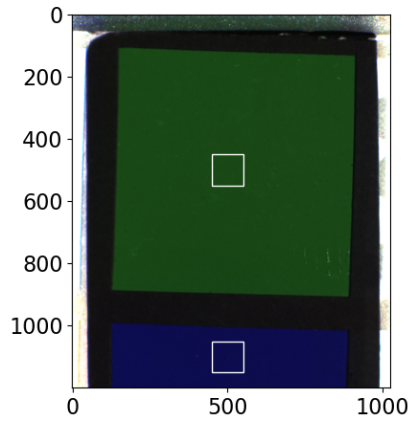

Figure 6: Reference reflectance as a function of test reflectance. The red line marks the optimal slope of 1, where the two reflectances would be in perfect agreement.

(a) Green

(b) Blue

(c) RGB reconstruction

Figure 7: Reflectance of the ColorChecker with the green and blue patches. The white squares on the RGB reconstruction denote the areas over which the test reflectances were averaged before plotting.

the same graph in Fig. 8(a), with the test reflectance averaged over a 100×100-pixel area for noise reduction. A reflectance colormap of the sample is shown in Fig. 8(b) with the area used for averaging marked on it as a white square.

The test reflectance curve shows similar deviations from the reference results as the in the rock sample– and ColorChecker measurements, with a dip in reflectance near 580 nm and a rise toward longer wavelengths. The sharp drop near 570 nm observed in Fig. 5(a) is likewise visible, though not to the same extent as in the rock sample measurement.

The most notable difference between the results of the ceramic samples and the other two sample types is that the test reflectance does not appear higher than the reference reflectance throughout the wavelength range. We suspect that this discrepancy is caused by a different measurement technique used to produce the reference reflectance, combined with a non-uniform sample surface. Reference reflectances of the two ceramic samples were measured using a PerkinElmer Lambda 1050 spectrophotometer equipped with an integrating sphere. The aperture of the sphere where the sample was placed only encompassed a small area on the sample. This measured area was likely not exactly the same where the HSI data was averaged to produce the presented reflectance curve. As such, it is possible that non-uniformities of the sample surface caused the two compared results to be measured from areas with different reflectance properties. Some of the possible non-uniformity is visible in Fig. 8(b), which presents a colormap of one reflectance frame. Some areas of the sample are brighter than others, indicating
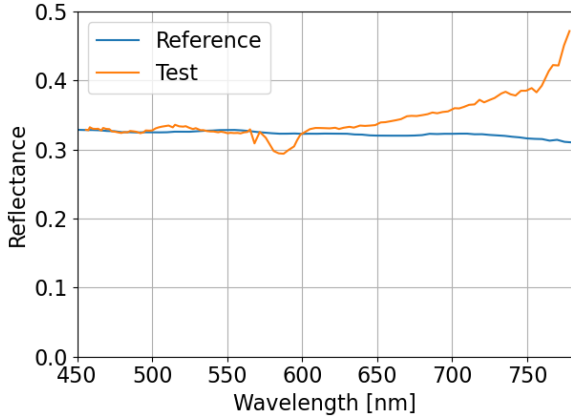
(a) Reflectance spectra
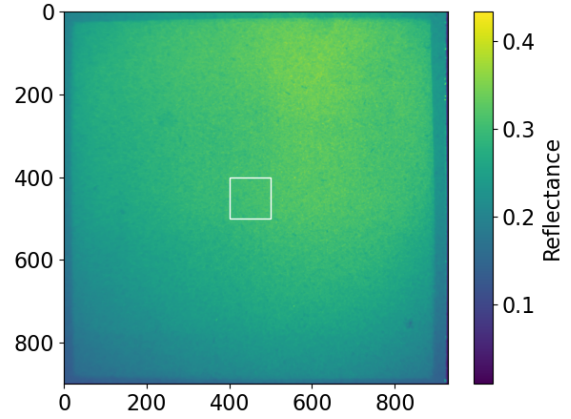
(b) Colormap of reflectance at $\lambda = 595$ nm

Figure 8: Reflectance of the lighter ceramic sample.

higher reflectance in this particular wavelength.

To summarize the results of the experiments, reflectances calculated with the proposed method deviated from reference results by unacceptable amounts. Especially problematic were the wavelengths in the red end of the spectrum and the area near 580 nm. In most measurements the test reflectances were also higher than the reference results throughout the whole wavelength range.

4. DISCUSSION

The proposed method of reflectance calculation provided erroneous results, but we believe the errors are caused by improper device calibration rather than the method itself. The comparison of spectral radiances measured with the HSI and the CS-2000 spectroradiometer, presented in Fig. 4, exhibit the same deviations as the reflectance results: higher readings throughout the wavelength range, a dip near 580 nm, and a rise in the red region. These errors in radiance propagate to the reflectances.

The objective lens of the used imager was exchangeable, and the objective and aperture size used in the original manufacturer calibration are unknown. Changing either of these will affect the radiance incident on the imager's sensor due to a change in acceptance angle. If the objective lens or the aperture was different in the calibration than in our measurements, this could cause the observed shift to higher radiance readings. If an adjustable aperture is also incorporated into a spacecraft-mounted FPI-HSI, its effects on recorded radiances must be considered during calibration. One must either make characterization measurements for all aperture sizes of the design or find a mathematical relation between aperture size and radiance incident on the sensor array.

The dip near 580 nm we attribute to overlapping quantum efficiencies of the sensor array's red, green, and blue pixels. Consider a frame taken with three peaks passing the FPI. For an ideal FPI-HSI of this type, the signal of the red pixels would only consist of the base wavelength, the green signal of only the first multiple of this wavelength, and the blue signal of only the second multiple. In our non-ideal imager, the sensitivities of the three pixel types overlap since the commercial CMOS-sensor used in the imager mimics the human eye's spectral sensitivity. This overlap causes all three types of pixels to also detect light from the two other peaks, in addition to light from the intended peak. This effect could also be the cause of the deviations seen in the red wavelengths.

As briefly discussed in Sec. 3, we believe the errors can be removed by proper calibration of the HSI. This assumption is supported by the similarity of spectral radiance deviations between the HSI and the spectroradiometer, seen in Fig. 4(b). Spectral radiances measured with the HSI deviate from the reference results, but the relative deviation is similar between the measurements, suggesting a linear relation between irradiance on the

sample and radiance measured with the HSI. This linearity implies that calibration of the device would not be overly difficult.

Analysis of asteroid compositions relies on evaluation of both spectral features and albedo. To retrieve the shape of reflectance spectra, absolute radiometric calibration is not necessarily needed: the spectra can be normalized, for example by setting the mean value to be 1. For albedo evaluation the absolute calibration is critical.

Minute changes in the operation of any measurement device can change the results it yields. It is generally a good practice to periodically re-calibrate any precision measurement device, including those onboard spacecraft. Proven approaches to this for spacecraft- based cameras and spectrometers include placing well-characterized light sources or reflectors on the spacecraft[7,8] Imaging these known samples and comparing the data to the characterization results can yield information on the instrument's performance, provided properties of the standards have not changed. This information, in turn, allows in-flight re-calibration of the instrument.

FPI-HSIs are no exception to this degradation of performance, especially when operating in the harsh environment of outer space. The sharp drop of reflectance at 570 nm seen in Fig. 5(a) was likely caused by a malfunction of the HSI, which is worrisome in this respect. If this type of error is typical to FPI-HSIs, it is important to know of its existence also in spacecraft–based sensors. However, the space– and mass capacity on a CubeSat platform is limited and may not allow installing calibration standards. Alternative methods of ensuring the imager performance should be explored.

While using a flat disc for the geometry of the imaginary white reference has merits in its simplicity, it will not give optimal results. Ideally, the white reference should be the same shape as the imaging target. For the proposed method of reflectance calculation this would require mapping the asteroid's surface geometry and overlaying this data with each captured radiance image. In the case of the Hera mission to Didymos, the surface geometry will be measured with a Light Detection and Ranging (LIDAR) instrument.[3] Taking subsequent images of a spinning asteroid from a moving spacecraft would also allow determining the geometry through photogrammetry. This latter approach may be more suitable for CubeSat missions since it does not require installing additional equipment on the spacecraft.

In our laboratory measurements, the dark current of the imager sensor was measured by placing a lens cap on the objective, capturing several frames, and calculating from them the average dark current of each pixel. In satellite applications, a similar approach based on a mechanical shutter may carry with itself some risks: if the shutter malfunctions, it can potentially render the whole HSI useless.

For missions where the FPI-HSI -equipped CubeSat is brought to the scene inside a larger mothercraft, like Milani inside Hera, the simplest solution for measuring the dark current may be to image the inside of the mothercraft. This approach could prove problematic, as over the lifetime of a mission the dark current may change due to temperature fluctuations or sensor degradation. The question of whether these effects are significant enough to merit introducing more complicated methods should be investigated.

Depending on the wavelength range of the FPI-HSI, one may be able to adjust the FPI cavity length so that all transmission peaks lie outside the bandpass filter's transmission area. The light reaching the sensor is then dependent on the FPI transmission outside of the peaks combined with the bandpass filter's transmission outside its passing wavelengths. With a high-finesse FPI and the right bandpass filter, the transmission of their combination could be approximately zero for some FPI cavity lengths. Capturing frames with such a cavity length could be used for measuring the dark current.

Still another approach would involve aiming the instrument away from the target asteroid and the Sun to observe the dark sky. Frames taken like this would also include light from the stars. Portions of such frames with no stars could be averaged to get one value for the sensor's dark current, but using this would ignore differences between the dark currents of different pixels. A more rigorous method would be to capture several frames with different imager orientations so that each pixel would have at least a few frames with no starlight incident on it.

Extending the wavelength range of imaging to infrared can offer further information on the composition of an asteroid, but infrared imaging also requires taking into account the effects of thermal emission. A part of the light arriving at an imager from an asteroid is not reflected sunlight, but blackbody radiation from the

surface warmed by absorbed solar radiation. For example, at the wavelength of 2.5 μm the thermal emission can contribute over 10 % of the recorded light for an object with an albedo of 0.15,[30] the assumed albedo of Didymos.[23] For accurate reflectance results, this thermal contribution of the recorded light must be evaluated and removed. In the OSIRIS–REx mission this was done by measuring the target asteroid with a separate point spectrometer, but this may not be a feasible solution for small CubeSat platforms with limited payloads.

Instead of direct measurements, the thermal emission could be modeled computationally by building a global map of the asteroid's surface temperature distribution. A simpler thermal model such as NEATM[31] will not be sufficient for spatially resolved measurements, as it only models the thermal radiation from a disc-integrated perspective. The temperature distribution on an asteroid's surface is known to be non-uniform. The Yarkovsky effect born from non-uniform distribution of radiated heat demonstrably causes observable changes to asteroid orbits.[32]

For further experiments, an FPI-HSI should be rigorously calibrated to record absolute radiances, and then used in a similar setup. If possible, the sample should also better represent an asteroid, making a meteorite more suitable than an arbitrary rock. Using the Sun as a light source would also bring the setup closer to the real situation of asteroid imaging, provided there is no cloud cover, and the weather conditions allow bringing measurement equipment outside.

5. CONCLUSIONS

A method for producing reflectance of asteroids from FPI-HSI data was suggested and tested in laboratory conditions. Measurements were made for three different types of samples, and the results of the proposed method were compared to reflectances produced with reference methods. For all three sample types, there were deviations between the test– and reference reflectances. However, we suspect these originated from improper calibration of the used imager rather than from errors in the proposed method. Further research is needed to confirm the performance of the method before applying it. Ideally, the imager of future measurements should be an FPI-HSI identical to one intended for CubeSat -use, and rigorously characterized and calibrated.

Other factors related to imaging asteroids with CubeSat-based FPI-HSIs, such as in-flight calibration, dark correction, and compensating for thermal emission, were also briefly considered. These problems have been solved for point-spectrometers, but the frame-based nature of the FPI-HSI and the limited space– and mass capacity of a CubeSat platform set some unique challenges. Since on these factors this work only gives suggestions not backed by measurements or simulations, more research is needed.

ACKNOWLEDGMENTS

REFERENCES

[1] Tilman, S., Doris, B., and Torrence, J., [*Encyclopedia of the Solar System*], Elsevier, 3rd ed. (2014).

[2] Gaffey, M. J., Burbine, T. H., and Binzel, R. P., "Asteroid spectroscopy: Progress and perspectives," *Meteoritics* **28**(2), 161–187 (1993).

[3] Michel, P., Kueppers, M., Sierks, H., Carnelli, I., Cheng, A. F., Mellab, K., Granvik, M., Kestilä, A., Kohout, T., Muinonen, K., Näsilä, A., Penttila, A., Tikka, T., Tortora, P., Ciarletti, V., Hérique, A., Murdoch, N., Asphaug, E., Rivkin, A., Barnouin, O., Bagatin, A. C., Pravec, P., Richardson, D. C., Schwartz, S. R., Tsiganis, K., Ulamec, S., and Karatekin, O., "European component of the aida mission to a binary asteroid: Characterization and interpretation of the impact of the dart mission," *Advances in Space Research* **62**(8), 2261–2272 (2018). Past, Present and Future of Small Body Science and Exploration.

[4] Xie, R., Bennett, N. J., and Dempster, A. G., "Target evaluation for near earth asteroid long-term mining missions," *Acta Astronaut.* **181**, 249–270 (2021).

[5] Sanchez, J. and McInnes, C., "Synergistic approach of asteroid exploitation and planetary protection," *Adv. Space Res.* **49**(4), 667–685 (2012).

[6] Bus, S. J., Vilas, F., and Barucci, M. A., "Visible-Wavelength Spectroscopy of Asteroids," in [*Asteroids III*], 169–182, University of Arizona Press (2002).

[7] Bell, J., Izenberg, N., Lucey, P., Clark, B., Peterson, C., Gaffey, M., Joseph, J., Carcich, B., Harch, A., Bell, M., Warren, J., Martin, P., McFadden, L., Wellnitz, D., Murchie, S., Winter, M., Veverka, J., Thomas, P., Robinson, M., Malin, M., and Cheng, A., "Near-ir reflectance spectroscopy of 433 eros from the nis instrument on the near mission: I. low phase angle observations," *Icarus* **155**(1), 119–144 (2002).

[8] Reuter, D. C., Simon, A. A., Hair, J., Lunsford, A., Manthripragada, S., Bly, V., Bos, B., Brambora, C., Caldwell, E., Casto, G., and et al., "The osiris-rex visible and infrared spectrometer (ovirs): Spectral maps of the asteroid bennu," *Space Sci. Rev.* **214** (Mar 2018).

[9] Golish, D. R., Drouet d'Aubigny, C., Rizk, B., DellaGiustina, D. N., Smith, P. H., Becker, K., Shultz, N., Stone, T., Barker, M. K., Mazarico, E., Tatsumi, E., Gaskell, R. W., Harrison, L., Merrill, C., Fellows, C., Williams, B., O'Dougherty, S., Whiteley, M., Hancock, J., Clark, B. E., Hergenrother, C. W., and Lauretta, D. S., "Ground and In-Flight Calibration of the OSIRIS-REx Camera Suite," *Space Sci. Rev.* **216**(1) (2020).

[10] Watanabe, S.-i., Tsuda, Y., Yoshikawa, M., Tanaka, S., Saiki, T., and Nakazawa, S., "Hayabusa2 mission overview.," *Space Sci. Rev.* **208**(1-4), 3 – 16 (2017).

[11] CubeSat program website. https://www.cubesat.org/about/. (Accessed: 2021-05-27).

[12] Freeman, A., "Exploring our solar system with CubeSats and SmallSats: the dawn of a new era," *CEAS Space Journal* **12**, 491–502 (Jan. 2020).

[13] Topputo, F., Wang, Y., Giordano, C., Franzese, V., Goldberg, H., Perez-Lissi, F., and Walker, R., "Envelop of reachable asteroids by m-argo cubesat," *Advances in Space Research* **67**(12), 4193–4221 (2021).

[14] ESA, "Hera mission to asteroid Didymos." https://www.esa.int/Safety_Security/Hera. (Accessed: 2021-05-02).

[15] Goldberg, H. R., Özgür Karatekin, Ritter, B., Herique, A., Tortora, P., Prioroc, C., Gutierrez, B. G., Martino, P., and Carnelli, I., "The Juventas CubeSat in Support of ESA's Hera Mission to the Asteroid Didymos," in [*Proceedings of the Small Satellite Conference*], **WKIV-05** (2019).

[16] Kohout, T., Näsilä, A., Tikka, T., Granvik, M., Kestilä, A., Penttilä, A., Kuhno, J., Muinonen, K., Viherkanto, K., and Kallio, E., "Feasibility of asteroid exploration using CubeSats—ASPECT case study," *Adv. Space Res.* **62**(8), 2239–2244 (2018).

[17] JPL Small-Body Database, "65803 Didymos (1996 GT)." https://ssd.jpl.nasa.gov/sbdb.cgi?sstr=2065803. (Accessed: 2021-04-26).

[18] Praks, J., Kestilä, A., Hallikainen, M., Saari, H., Antila, J., Janhunen, P., and Vainio, R., "Aalto-1 - An experimental nanosatellite for hyperspectral remote sensing," *Int. Geosci. Remote Sens. Symp.* (July), 4367–4370 (2011).

[19] Reaktor Space Lab, "Reaktor Hello World." https://reaktorspace.com/reaktor-hello-world/. (Accessed: 2021-08-10).

[20] Saari, H., Aallos, V.-V., Akujärvi, A., Antila, T., Holmlund, C., Kantojärvi, U., Mäkynen, J., and Ollila, J., "Novel miniaturized hyperspectral sensor for UAV and space applications," in [*Sensors, Systems, and Next-Generation Satellites XIII*], Meynart, R., Neeck, S. P., and Shimoda, H., eds., **7474**, 517 – 528, International Society for Optics and Photonics, SPIE (2009).

[21] Saari, H., Pölönen, I., Salo, H., Honkavaara, E., Hakala, T., Holmlund, C., Mäkynen, J., Mannila, R., Antila, T., and Akujärvi, A., "Miniaturized hyperspectral imager calibration and UAV flight campaigns," in [*Sensors, Systems, and Next-Generation Satellites XVII*], Meynart, R., Neeck, S. P., and Shimoda, H., eds., **8889**, 448 – 459, International Society for Optics and Photonics, SPIE (2013).

[22] Manolakis, D. G., Lockwood, R. B., and Cooley, T. W., [*Hyperspectral Imaging Remote Sensing: Physics, Sensors, and Algorithms*], Cambridge University Press (2016).

[23] Ferrari, F., Franzese, V., Pugliatti, M., Giordano, C., and Topputo, F., "Preliminary mission profile of hera's milani cubesat," *Adv. Space Res.* **67**(6), 2010–2029 (2021).

[24] NREL, "ASTM Standard Extraterrestrial Spectrum Reference E-490-00." https://www.nrel.gov/grid/solar-resource/spectra-astm-e490.html. (Accessed: 2021-04-26).

[25] Eskelinen, M. A. and Hämäläinen, J., "Fpipy Python library." Available online: https://github.com/silmae/fpipy (visited on 2021-05-04) (2019).

[26] Konica Minolta, "CS-2000 spectroradiometer." https://sensing.konicaminolta.asia/product/spectroradiometer-cs-2000/. (Accessed: 2021-04-15).

[27] PerkinElmer Lambda 1050 spectrophotometer. https://www.perkinelmer.com/product/lambda-1050-2d-system-l6020056. (Accessed: 2021-05-09).

[28] Harris, C. R., Millman, K. J., van der Walt, S. J., Gommers, R., Virtanen, P., Cournapeau, D., Wieser, E., Taylor, J., Berg, S., Smith, N. J., Kern, R., Picus, M., Hoyer, S., van Kerkwijk, M. H., Brett, M., Haldane, A., Fernández del Río, J., Wiebe, M., Peterson, P., Gérard-Marchant, P., Sheppard, K., Reddy, T., Weckesser, W., Abbasi, H., Gohlke, C., and Oliphant, T. E., "Array programming with NumPy," *Nature* **585**, 357–362 (2020).

[29] Lind, L., *Fabry–Perot -based hyperspectral reflectance imaging of asteroids*, Master's thesis, University of Eastern Finland (2021).

[30] Rivkin, A., Binzel, R., and Bus, S., "Constraining near-earth object albedos using near-infrared spectroscopy," *Icarus* **175**(1), 175–180 (2005).

[31] Harris, A. W., "A thermal model for near-earth asteroids," *Icarus* **131**(2), 291–301 (1998).

[32] Chesley, S. R., Ostro, S. J., Vokrouhlický, D., Čapek, D., Giorgini, J. D., Nolan, M. C., Margot, J.-L., Hine, A. A., Benner, L. A. M., and Chamberlin, A. B., "Direct detection of the yarkovsky effect by radar ranging to asteroid 6489 golevka," *Science* **302**(5651), 1739–1742 (2003).